SCIENCE CHINA Materials

ARTICLES

mater.scichina.com link.springer.com

Published online 16 April 2018 | https://doi.org/10.1007/s40843-018-9254-6

Sci China Mater 2018, 61(12): 1575–1586

Co_3O_4 nanosheet-built hollow dodecahedrons *via* a two-step self-templated method and their multifunctional applications

Yuanyuan Li[1,2], Bo Liu[1,2], Hong Wang[1,2], Xingsong Su[1,2], Lei Gao[1], Fei Zhou[1] and Guotao Duan[1*]

ABSTRACT **The Co_3O_4 nanosheet-built hollow dodecahedrons (Co_3O_4 NSHDs) were fabricated *via* a controllable two-step self-templated method. The ZIF-67 dodecahedrons were prepared as first self-template to synthesize the Co-LDH hollow dodecahedrons, which were further used as self-template to fabricate Co_3O_4 NSHDs by a controlled calcination. The proposed two-step self-templated method not only brings hollow structures without auxiliary template, ultrathin nanosheet, ultrafine grains, and large surface areas, but also allows the easy and uniform surface modification, as demonstrated of PdO modification. The Co_3O_4 NSHDs with above features could show multifunctional applications, such as sensing and catalysis. Experiments suggest that the Co_3O_4 NSHDs show good gas sensing performances to trimethylamine at a low operating temperature (100°C). They can be further enhanced by PdO surface modification, which have a low detection limit (250 ppb) and a short response time (4.5 s). In addition, the Co_3O_4 NSHDs exhibited excellent oxygen evolution reaction performances with a low overpotential of 359 mV, low Tafel slope of 80.7 mV dec^{-1} and low electrochemical impedance, which was superior to those for the Co_3O_4 NCs obtained by directly calcinating the ZIF-67 templates, Ni foam and most common metal oxides catalysts.**

Keywords: Co_3O_4, self-templated method, gas sensing, oxygen evolution reaction

INTRODUCTION

Hollow nanostructures have drawn continuous attentions because of their novel structural merits of anti-expansion capacity and large surface areas, which would find potential applications in various fields such as gas sensing and catalysis [1–4]. For example, Tian and co-workers synthesized the hollow Fe_2O_3 nanoboxes with excellent gas sensing performance to H_2S [5]. He and co-workers [6] synthesized the nanocomposite NiCoP/C nanoboxes with an enhanced electrochemical performance as a catalyst for oxygen evolution reaction (OER). In general, hollow nanostructures are fabricated based on auxiliary template such as polystyrene or carbon colloidal spheres [7–9], which includes two processes of material growth on auxiliary template and then the removal of template. Obviously, auxiliary templated method is able to realize size control, while bringing fussy fabrication process and high cost. Therefore, finding a facile and low-cost method without auxiliary template to synthesize hollow nanostructures is still a challenge now.

The zeolitic imidazolate frameworks (ZIFs), a subnet of metal organic frameworks, have been intensively studied in recent years owing to huge surface areas, regular morphology, and chemical robustness [10–12]. Especially, ZIFs are often used as raw material to directly synthesize hollow nanostructures [13–15]. For example, Jiang *et al.* [16] have synthesized ZnS hollow polyhedron with Zn-containing ZIF-8. Shao and co-workers [17] have synthesized Co_3O_4 hollow dodecahedrons with ZIF-67. Therefore, ZIFs are an ideal self-template to synthesize hollow nanostructures without auxiliary template.

On the other hand, layered double hydroxides (LDHs), which are an emerging class of lamellar functional materials with brucite-type layers, have also received great attention [18–21]. LDHs have many fascinating properties, such as large surface areas and more active sites owing to its lamellar structure. It could remain the original structure after thermal treatment and be easily modified by the nanoscale metal nanoparticles (NPs) with

[1] Key Lab of Materials Physics, Anhui Key Lab of Nanomaterials and Nanotechnology, Institute of Solid State Physics, Chinese Academy of Sciences, Hefei 230031, China

[2] University of Science and Technology of China, Hefei 230026, China

[*] Corresponding author (email: duangt@issp.ac.cn)

a uniform particle size and high dispersion. With these advantages, LDHs are not only widely applied in various fields such as catalysts, supercapacitors, but also used as supports or precursors to further fabricate the functional materials [22–24]. For example, Gao *et al.* [25] reported that Mg-Al-CO_3 LDH-derived mixed metal oxides were applied for high-temperature CO_2 capture. However, the sensing performances of metal oxides obtained from the LDHs precursor have not been well studied.

In our paper, combining the characteristic of ZIFs and LDHs, the Co_3O_4 nanosheet-built hollow dodecahedrons (Co_3O_4 NSHDs) were fabricated *via* a controllable two-step self-templated method. Firstly, we choose ZIF-67 as a self-template to synthesize Co-LDH hollow nanostructures (Co-LDH HDs). On the one hand, ZIF-67 can be easily removed in acidic solutions and cobalt ions with variable valences can provide trivalent ions to LDHs. On the other hand, cobalt element in ZIF-67 derived Co_3O_4 has been applied in many fields such as gas sensing and catalyst owing to its semiconductor characteristic and high catalytic activity caused by good vacant electron orbit [26–32]. Secondly, Co-LDH HDs were further used as self-template to fabricate Co_3O_4 NSHDs by a controlled calcination. This two-step self-templated method not only brings hollow structures without auxiliary template, ultrathin nanosheet, ultrafine grains, and large surface areas, but also allows the easy and uniform surface modification of Co_3O_4 NSHDs. The Co_3O_4 NSHDs with well-distributed PdO NPs could be obtained by this Pd modified Co-LDH HDs based on heat treatment. The as-prepared Co_3O_4 NSHDs with above features may find multifunctional properties and applications. In this paper, their applications in trimethylamine (TMA) detection and OER catalysis were studied in detail.

EXPERIMENTAL SECTION

Cobalt nitrate hexahydrate ($Co(NO_3)_2.6H_2O$), methanol (CH_3OH), ethanol (C_2H_5OH), sodium borohydride ($NaBH_4$), palladium chloride ($PdCl_2$), potassium hydroxide (KOH) were purchased from Sinopharm Chemical Regent Co., Ltd. 2-methylimidazole (MeIm, $C_4H_6N_2$) was purchased from Aldrich. All the reagents were used without further purification.

ZIF-67 was synthesized by precipitation reaction at room temperature [15]. Typically, 0.291 g of cobalt nitrate hexahydrate and 0.328 g of 2-methylimidazole were each dissolved in 25.0 mL methanol. These two solution were mixed and stirred continuously for 30 min. After static setting for 24 h, the precipitate was separated by centrifugation (6,000 rpm) and washed with ethanol for three times. Finally, the violet powder was obtained after drying at 60°C. Co_3O_4 powders were produced by the calcination of ZIF-67 powders at 400°C for 1 h with a heating rate of 2°C min^{-1}.

First, 30 mg of ZIF-67 nanocrystals was dispersed into 20 mL of ethanol. Then 5 mL of ethanol solution containing 100 mg $Co(NO_3)_2$ was added. And the mixture was stirred for 1 min. Then the reaction vessel was put into an ultrasonic bath for 90 min [15]. Finally, the Co-LDH HDs was purified by centrifugation at 8,000 rpm and washed with ethanol for several times. The Co-LDH HDs powder was obtained by drying at 60°C for 12 h. To synthesize the PdO functioned Co_3O_4-nanosheet HDs, the Pd NPs were modified on the surface of Co-LDH HDs by the infiltration and reduction process. 30 mg of Co-LDH HDs was dispersed in 10 mL of deionized water. Then, Na_2PdCl_2 was dissolved in above dispersion and Pd metal ions were reduced by $NaBH_4$ solution (1 mmol L^{-1}). After this process, Pd NPs modified Co-LDH HDs were separated by repeated centrifugation (6,000 rpm) and washed with ethanol for three times. The obtained Pd NPs modified Co-LDH HDs were dried at 60°C for 8 h. PdO functioned Co_3O_4-nanosheet HDs were obtained by the calcination of Pd modified Co-LDH HDs at 300°C for 1 h with a heating rate of 2°C min^{-1}. To determine the optimum conditions, synthetic experiments with different calcination temperatures from 300 to 500°C were conducted and the resulting products were denoted as Co_3O_4-300°C, Co_3O_4-400°C, and Co_3O_4-500°C.

The morphologies and microstructures of the products were characterized with field-emission scanning electron microscopy (FESEM, Srion200) and high-resolution transmission electron microscopy (HRTEM). The crystallographic structures of the samples were carried on a Philips X'pert powder X-ray diffracometer (XRD) using Cu Kα radiation (λ=0.15419 nm). The specific surface area of the products was measured by the Brunauer-Emmett-Teller (BET) method using nitrogen adsorption and desorption isotherms on a Micromeritics Instrument Corporation sorption analyzer (TriStar II 3020). X-ray photoelectron spectroscopy (XPS) was performed on a Perkin-Elmer model PHI 5600 XPS system from a monochromatic aluminum anode X-ray source with Kα radiation (1,486.6 eV), and the spectra were calibrated with the C 1s peak at 284.6 eV as an internal standard. Thermogravimetry analysis (TGA) was carried out using the thermogravimetry equipment (Perkin-Elmer Corporation, Pyris 1) in the temperature range from 50 to 700°C at a heating rate of 10°C min^{-1} in air. The Raman spectra were carried on the Renishaw 2000 laser Raman

microscope with argon ion laser at 785 nm excitation. The laser power is 2 mW, and the spot size is 1 μm.

The samples were mixed with ethanol to form paste, and the density of samples is 50 g L^{-1}. Subsequently the paste was coated on the interdigital electrodes which were patterned with two parallel Au electrodes on the front side and a Pt microheater on the back side, as shown in the inset of Fig. S1b. Gas sensing measurements were carried out at different temperatures. After coating the sensing materials, we choose a sensor based on our sensing materials to measure the temperature at different voltage using thermocouple by changing the voltage of Pt microheater using a DC power supply (Agilent models U3606A and U8002A) (Fig. S1a). Considering the potential impact of thermocouples on the sensor, this sensor will not be used for gas sensing. Measured temperature data with variation of voltage using above method can be applied in other sensors based on the identical conditions and materials. Therefore, comparing with the measured temperature data, the operating temperature can be controlled by changing the voltage of Pt microheater using a DC power supply. Before testing, the sensor was aged in air with a humidity level of about 50% for 24 h at 200°C to achieve the device stabilization.

All gas response measurements were carried out in air with a humidity level of about 50%. The gas sensing experiments were carried out in a home-built static testing system with a multimeter/DC power supply. After target gas with different concentrations was injected into the gas chamber (Fig. S1b), the resistance of the sensor will be changed. The internal volume of the chamber was 20 L and the uniformity of the gas and flow of the air can be realized by installing two mini fans in the chamber. Four sensors could be placed in the chamber at a time for simultaneous monitoring. When the resistance of sensor reached a constant value, the gases were taken out. The sensitivity of sensors is defined as R_g/R_{air}, where R_{air} and R_g are the resistances of the sensor before and after exposure to the target gases, respectively. The response time is expressed as the time required for the sensor to achieve 90% of the total resistance change in the case of response. The recovery time is defined as the time for falling to 10% of its maximum response after testing gas gets out.

Electrochemical measurements of the samples were performed in 1.0 mol L^{-1} KOH solution (pH=14) after purging the electrode with O_2 for 30 min with *iR*-correction using a standard three-electrode system. Ni foam modified with the electrocatalyst, a Pt wire, and an Ag/AgCl electrode are used as working electrode, counter-electrode, and reference electrode, respectively. The catalyst suspensions containing 250 μL water, 250 μL ethanol, 10 mg catalyst and 40 μL 5 wt% Nafion solutions were obtained by ultrasonic mixing for about 30 min. 100 μL of the catalyst ink suspension obtained onto the Ni foam and then it was left to dry under infrared light. The potential *versus* the reversible hydrogen electrode (RHE) can be obtained from the potential, measured against a SCE electrode, according to $E_{vs.RHE} = E_{vs.SCE} + E^{\theta}_{SCE} + 0.059pH$. Overpotential ($\eta$) for the OER was $\eta = E_{vs.RHE} - 1.23\ V = E_{vs.SCE} - 0.207\ V$ [33].

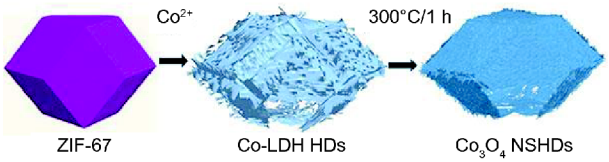

Figure 1 The schematic preparation process of Co_3O_4 NSHDs.

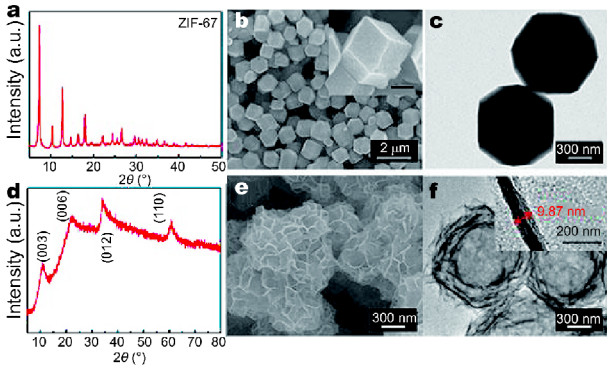

Figure 2 (a) XRD pattern of ZIF-67. (b) SEM image of ZIF-67, and the inset is a corresponding magnified SEM image. (c) TEM image of ZIF-67. (d) XRD pattern of Co-LDH HDs. (e) SEM image of Co-LDH HDs. (f) TEM image of Co-LDH HDs.

RESULTS AND DISCUSSION

Fig. 1 shows the schematic of the preparation of Co_3O_4 NSHDs. First, ZIF-67 templates were fabricated by mixing cobalt nitrate and MeIm in methanol. Then, Co_3O_4 NSHDs were produced by calcinating the Co-LDH HDs fabricated by adding extra cobalt nitrate. The XRD pattern indicates that the as-synthesized ZIF-67 is phase-pure (Fig. 2a) [34]. The SEM and TEM images show that ZIF-67 is rhombic dodecahedron and exhibit a homogeneous particle size of ~800 nm (Fig. 2b, c).

From the XRD pattern (Fig. 2d), all of the diffraction peaks (003), (006), (012), and (110) are coincident with the microstructure of a typical Co-LDH which has been previously reported [15]. As we all know, XPS measures

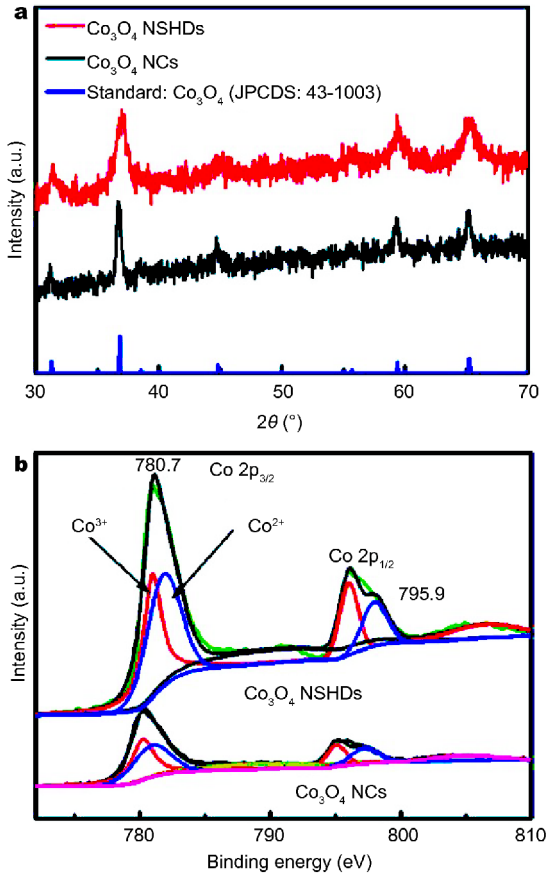

Figure 3 (a) XRD patterns and (b) XPS data of the as-prepared Co_3O_4 NCs and Co_3O_4 NSHDs.

the energy distribution of samples' electrons by irradiating samples using monochromatic radiation to induce electron excitation of the atoms or molecules of samples. According to the literature, the Co 2p core lines of $Co(OH)_2$ are divided into Co $2p_{1/2}$ (797.6 eV) and Co $2p_{3/2}$ (781.6 eV) main peaks [35]. Due to the existence of Co^{3+} in Co-LDH, Co $2p_{1/2}$ and Co $2p_{3/2}$ main peaks of Co-LDH shift to lower energy regions (Fig. S2), indicating the existence of Co^{3+} [15]. The morphology and hollow structure are characterized using the SEM and TEM images of the LDH samples, as shown in Fig. 2e, f. The SEM image shows that LDH samples inherit the dimension of the ZIF-67 templates and are assembled to a polyhedral shell with nanosheets. The inner cavity can be clearly revealed by the shells and the hollow interiors as shown in TEM image. From the magnified TEM image, the LDH samples consists of thin nanosheets approximately 9.87 nm in thickness. These results clearly indicate the formation of Co-LDH hollow dodecahedrons (Co-LDH HDs) with ultrathin nanosheets.

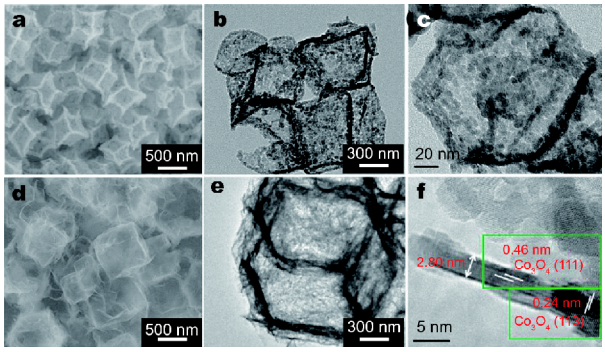

Figure 4 (a–c) SEM, TEM and HRTEM images of Co_3O_4 NCs, respectively. (d–f) SEM, TEM and HRTEM images of Co_3O_4 NSHDs, respectively.

By calcinating Co-LDH HDs and ZIF-67 at optimized temperature, black powders were obtained respectively. The XRD patterns of the two samples are shown in Fig. 3a. The diffraction peaks of these two samples are corresponding well to the characteristic peaks of standard Co_3O_4 (JPCDS: 43-1003), which verifies the formation of Co_3O_4 with cubic spinel structure [36]. Two major Co 2p XPS peaks (Fig. 3b) of the two samples at around 795.9 and 780.7 eV, corresponding to the Co $2p_{1/2}$ and Co $2p_{3/2}$ spin orbit peaks of Co_3O_4, indicates that Co-LDH HDs and ZIF-67 have completely converted to Co_3O_4. SEM and TEM images show the Co_3O_4 particles retain the similar size and shape. Compared with the ZIF-67, however, the surface of these particles is rough and decorated with tiny holes with numerous grains. Another Co_3O_4 sample with Co-LDH HDs templates has the similar size and shape as the Co-LDH HDs precursors approximately 800 nm and is assembled to a polyhedral shell with nanosheets (Fig. 4d, f). From the TEM image (Fig. 4e), no collapse was found for the hollow dodecahedrons after annealing. The HRTEM image (Fig. 4f) indicates that Co_3O_4 sample is composed of ultrafine nanosheets approximately 2.80 nm in thickness, and shows the high crystalline with a lattice fringes of 0.24 nm (d_{311}) and 0.48 nm (d_{111}). Obviously, the thickness of Co_3O_4 nanosheets with numerous interconnected ultrafine grains is smaller than that of Co-LDH nanosheets, which may be attributed to dehydration of Co-LDH during annealing.

Co_3O_4 NSHDs can be successfully synthesized owing to the successful preparation of the precursor Co-LDH HDs and the selection of the subsequent annealing temperature. On the one hand, the precursor Co-LDH HDs can be successfully synthesized with ZIF-67 templates by adding a moderate amount of cobalt nitrate for two reasons. Firstly, as the cobalt ions hydrolyze, acids gen-

erate in the reaction and etch the ZIF-67 templates. Secondly, cobalt ions with variable valences can provide trivalent ions to LDHs. These results have been reported in the literature [15]. Therefore, the preparation of perfect hollow structure depends on the control of the Co-LDH growing and the ZIF-67 etching. When the concentration of $Co(NO_3)_2.6H_2O$ is low, the ZIF-67 cannot be completely etched due to very weak acidic environment. When the concentration of $Co(NO_3)_2.6H_2O$ is high, the ZIF-67 can be completely etched, resulting in an excess of Co-LDH in the solution. From the TEM images (Fig. S3), the separate precipitation is obvious as the concentration of $Co(NO_3)_2.6H_2O$ was increased.

On the other hand, we found that selecting an appropriate calcination condition is critical for the synthesis of the Co_3O_4 NCs and Co_3O_4 NSHDs. The Co_3O_4 NCs was obtained successfully at 300°C calcination temperature, as previously reported [35]. The thermal behavior of Co-LDH HDs was scrutinized, indicating that Co-LDH HDs can completely transfer to Co_3O_4 at around 300°C and over (Fig. S4a). It is easily understood that the size of grains will increase as the calcination temperature increases. However, large grains not only possibly cause structural collapse but also affect the performances of the material. For better understanding, the calcination of Co-LDH HDs was performed at 300, 400 and 500°C for 1 h in air. The XRD analysis of the three samples obtained at different calcination temperatures clearly showed their spinel structure of Co_3O_4 (JPCDS: 43-1003) (Fig. S4b). The SEM images are shown in Fig. 5a–f. With the calcination temperature increase, no collapse was found for the whole structure of hollow dodecahedron. However, from the magnified SEM images, the nanosheets gradually collapse due to the growth of the grains at high calcination temperature. According to the literature, nanosized grains can enhance the strain to cause a Raman shift toward low wavenumbers [36], which was also proven in our case (Fig. 6). With the calcination temperature increase, an obvious blue shift can be observed in all of the Raman peaks for the three Co_3O_4 samples. Typically, the strongest peak assigned to A1g shifts from 673 cm^{-1} (300°C) to 676 cm^{-1} (400°C), and 683 cm^{-1} (500°C). These results correspond to the large Co_3O_4 grains at a high calcination temperature. As is known, decreasing the grain size of the gas sensing film can improve the gas sensing response of p-type semiconductors [37]. The Co_3O_4 NSHDs obtained at 300°C calcination temperature composed of numerous ultrafine grains may exhibit enhanced sensing performances.

Larger surface areas with numerous mesoporous can provide higher surface activity and more active sites for surface reactions, which will enhance the gas sensing and catalytic reductions. As shown in Fig. 7, b, the Co_3O_4 NCs and Co_3O_4 NSHDs possess BET surface areas of 54.209 and 98.837 $m^2\ g^{-1}$, respectively. In addition, from the N_2 desorption measurements, the corresponding pore diameter distributions by BJH pore size distribution analysis are obtained, as shown in Fig. 7c, d. The results indicate that average pore sizes of the two samples are 6.5 and 2.44 nm, respectively. The BJH adsorption cumulative volume of pores of the Co_3O_4 NCs and Co_3O_4 NSHDs between 17 and 3,000 Å are 0.15 and 0.43 $cm^3\ g^{-1}$, respectively. These results indicate that the Co_3O_4 NSHDs have nearly twice higher surface area of the Co_3O_4 NCs, which is also larger than most of the previously reported porous Co_3O_4 nanostructures [38–39]. At the same time, the Co_3O_4 NSHDs have smaller pores and larger volume of pores than Co_3O_4 NCs, which means that Co_3O_4 NSHDs have more mesopores than Co_3O_4 NCs. Co_3O_4 NSHDs with larger surface area and more mesopores could provide more active sites, facilitate the transport of gas molecules or electrons/ions to the active sites and improve their sensing and catalytic performances.

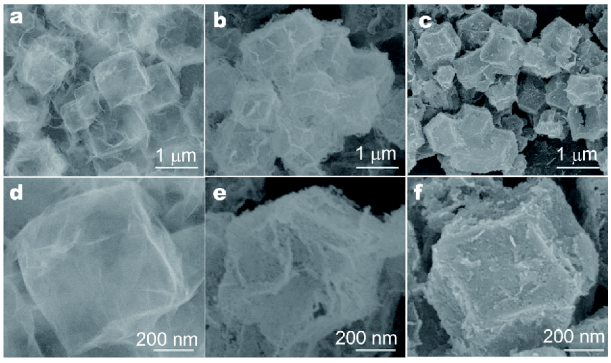

Figure 5 SEM images of Co_3O_4 samples obtained at 300°C (a, d), 400°C (b, e) and 500°C (c, f) calcination temperatures.

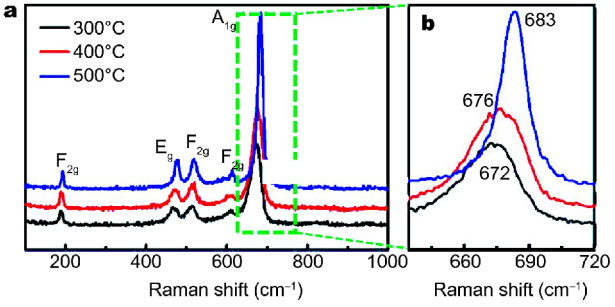

Figure 6 (a) Raman spectra of the Co_3O_4 samples obtained at 300°C, 400°C and 500°C calcination temperatures, respectively; (b) corresponding high-resolution Raman spectra of the A_{1g} active peaks.

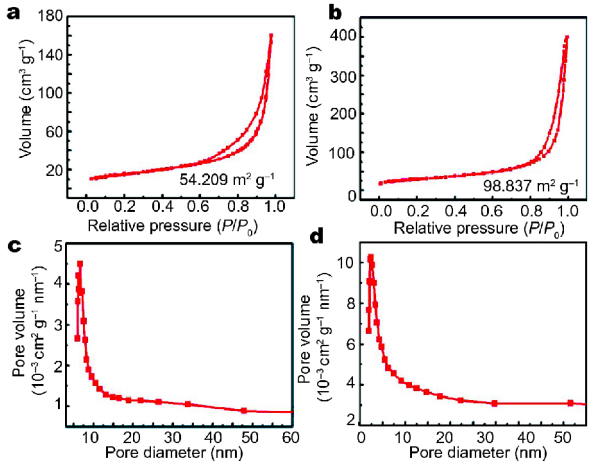

Figure 7 N_2 adsorption-desorption curves and pore size distributions of as-prepared Co_3O_4 NCs (a, c) and Co_3O_4 NSHDs (b, d).

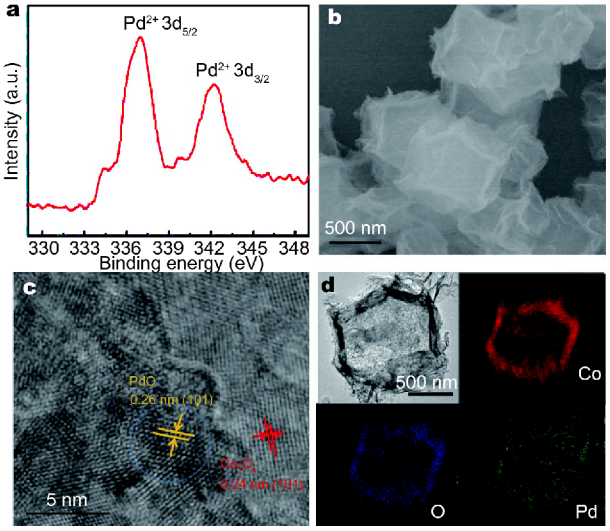

Figure 8 (a) XPS data, (b) SEM image, (c) HRTEM image, and (d) elemental maps of Co, O and Pd of PdO-Co_3O_4 NSHDs, respectively.

On the other hand, LDHs can provide a confined and stable microenvironment for the *in situ* synthesis of metal NPs onto LDHs' surface owing to the ordered arrangement of the cationic reductant in the LDH layers. The uniform modification of Co_3O_4 NSHDs can be easily achieved using Co-LDH HDs templates. In our work, firstly, the nanoscale Pd particles were easily modified on the surface of Co-LDH HDs by reduction. The XPS data (Fig. S5a) indicate that the two major peaks located at 336.1 and 341.4 eV were corresponding to Pd $3d_{5/2}$ and Pd $3d_{3/2}$, respectively, which confirmed the formation of Pd NPs [40]. The synthesized Pd-Co-LDH HDs exhibited similar hollow dodecahedrons structure of Co-LDH HDs with the average size of 800 nm, as shown in SEM image (Fig. S5b). The energy dispersive X-ray spectroscopy (EDS) elemental mapping images (Fig. S5c) clearly confirmed the existence and high dispersibility of Pd element in Co-LDH HDs, indicating that nanoscale Pd NPs were uniformly prepared and modified on the Co-LDH HDs. On the other hand, Pd-Co-LDH HDs were transformed to PdO functioned Co_3O_4 NSHDs after calcination at 300°C in air. The XPS data (Fig. 8a) indicates that the two major peaks located at 337 and 342.2 eV were corresponding to Pd^{2+} $3d_{5/2}$ and Pd^{2+} $3d_{3/2}$, respectively, which the modified Pd NPs were oxidized to PdO during the calcination [40]. The PdO modified Co_3O_4 NSHDs exhibited similar hollow dodecahedrons structure to that of Co_3O_4 NSHDs with the average size of 800 nm, as shown in Fig. 8b. The HRTEM image clearly shows the PdO NPs (3–4 nm) with the lattice fringe of PdO (101) plane and Co_3O_4 with the lattice fringe of Co_3O_4 (311) plane, as shown in Fig. 8c. The EDS images clearly indicate that nanoscale PdO NPs were uniformly modified on the Co_3O_4 NSHDs, as shown in Fig. 8d. The uniform modification of PdO could improve the performances of the materials, such as sensing performances in the next section. We believe that uniform modification of other NPs on the Co_3O_4 NSHDs could also be achieved by this way.

Based on the large surface areas, numerous mesopores, ultrafine grains, easy functionalization characteristics, Co_3O_4 NSHDs/PdO-Co_3O_4 NSHDs are supposed to be effective in detecting volatile organic compounds. As we all know, TMA is a type of poisonous and harmful malodorous gases in various fields, such as food industries, environmental health, and has adverse effects on the ecological environment and human health [41–42]. So the detection of TMA is very important.

In our work, the detailed sensing performances of the Co_3O_4 NSHDs/PdO-Co_3O_4 NSHDs for TMA were investigated. As we all know, most of TMA gas sensors devices were operated at high temperatures (300–450°C) [43–45]. The sensing measurements based on our materials can be carried out at low operating temperature (100°C) and showed excellent sensing performances. Gas sensing measurements were performed by exposing the obtained sensor based on PdO-Co_3O_4 NSHDs to 5 ppm TMA gas at different operating temperatures to determine the optimum conditions, as shown in Fig. S6. The highest gas response (4.5) was observed at 100°C. Fig 9a shows the responses of Co_3O_4 NCs, Co_3O_4 NSHDs and PdO-Co_3O_4 NSHDs towards same concentration TMA at 100°C. The results show that PdO-Co_3O_4 NSHDs have higher sensing response (R_g/R_{air}=15.04) than Co_3O_4 NSHDs (R_g/R_{air}=4.38) and Co_3O_4 NCs (R_g/R_{air}=1.79). Two

enhancement effects were clearly shown: one is from the Co_3O_4 NSHDs with hollow structure, larger surface areas and ultrafine grains; the other is from PdO NPs surface modification. We also investigated the influence of loading amounts of PdO NPs on the sensing performances. Three Co_3O_4 NSHDs samples with different loading amounts were prepared for TMA sensing measurement. As shown in Fig. S7, the PdO-Co_3O_4 NSHDs sensor with 2.5 wt% PdO exhibits the highest TMA sensing performance, which will be selected for the subsequent gas sensing measurement.

We further investigated the dynamic sensing characteristics of Co_3O_4 NSHDs and PdO-Co_3O_4 NSHDs at 100°C, as shown in Fig. 9b. It can be found that PdO-Co_3O_4 NSHDs detect the 250 ppb of TMA in the actual test with the noticeable sensing response value (R_g/R_{air} = 2.26). It is important to mention that the detection limit (250 ppb) was lower than that of Co_3O_4 NSHDs (1 ppm), as shown in Fig. S8. This lower detection limit could endow the sensors with abilities for application in TMA detection and promote their potential in commercial applications. Moreover, a fitting curve (the inset in Fig. 9b) of the sensing response *versus* the TMA gas concentration was easily obtained, and the linear correction coefficient is 0.95, indicating the good linearity, which is advantageous for TMA gas quantity analysis in practical application. These results imply that the uniform modification of PdO NPs not only improves the sensing response, but also decreases the detection limit.

The reproducibility and reliability of PdO-Co_3O_4 NSHDs to TMA were further studied. The responses are almost unchanged during the sensor operation for five cycles, implying a good stability of PdO-Co_3O_4 NSHDs. In addition, the sensor shows a very short response time and recovery time of 4.5 s and 12.5 s, respectively. The selectivity of Co_3O_4 NSHDs and PdO-Co_3O_4 NSHDs were further investigated by sensing measurement for various analytes such as methyl sulfide, styrene, dimethyl sulfide, ethanol, acetone, CS_2, H_2S and methanethiol, as shown in Fig. 9d. The sensing responses of PdO-Co_3O_4 NSHDs towards all gases for same concentration are higher than that of Co_3O_4 NSHDs and their selectivity to TMA gas does not change, which means that the existence of PdO has no effect on selectivity. Although the PdO-Co_3O_4 NSHDs exhibited highest TMA sensing response (R_g/R_{air} =8.23), the sensing responses toward other gases are also

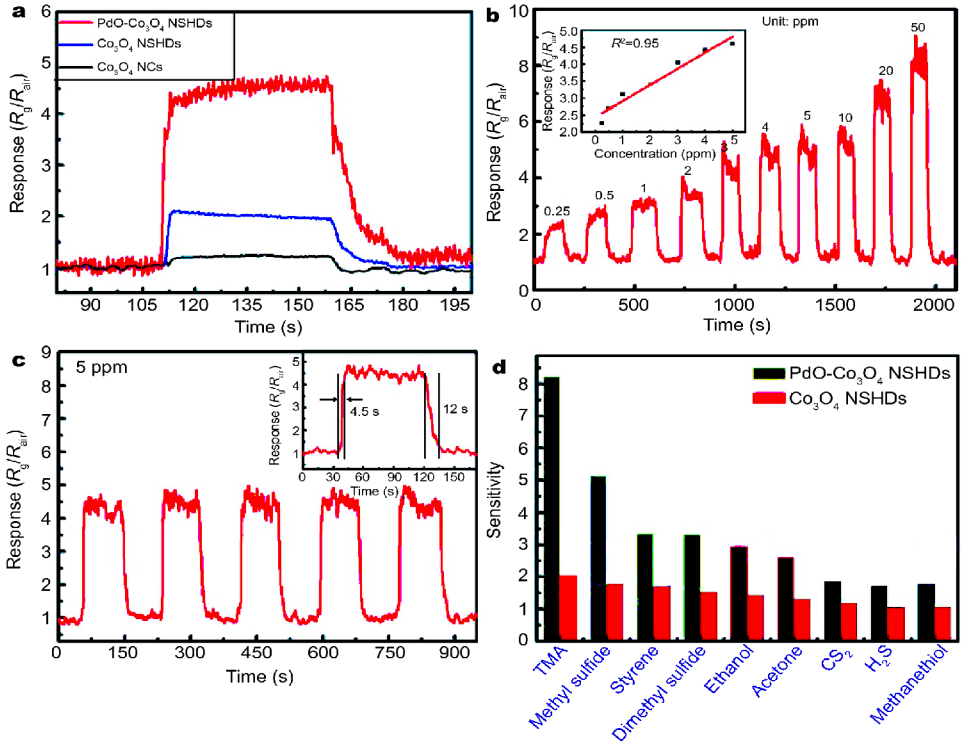

Figure 9 (a) Sensing responses of the three samples to 5 ppm TMA at 100°C. (b) Dynamic TMA sensing transient properties of PdO-Co_3O_4 NSHDs in the concentration range of 0.25–50 ppm. The inset in (b) is the relationship between response and TMA concentration. (c) Cyclic sensing transient of PdO-Co_3O_4 NSHDs toward 5 ppm of TMA. (d) Response values of Co_3O_4 NSHDs and PdO-Co_3O_4 NSHDs to 50 ppm of interfering analytes.

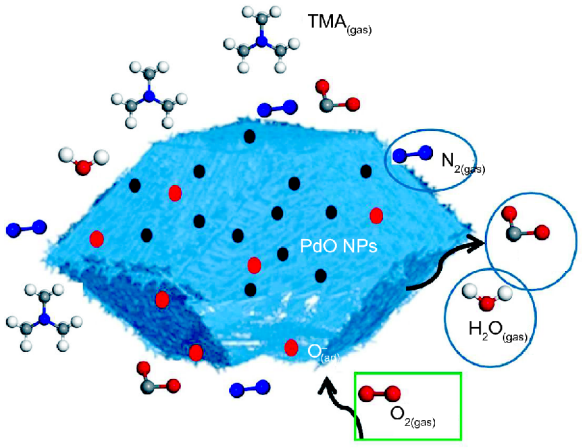

Figure 10 Schematic illustration of TMA sensing mechanism for PdO-Co_3O_4 NSHDs.

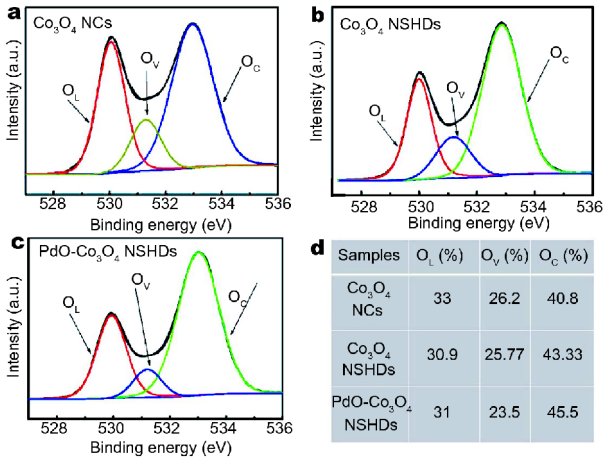

d

Samples	O_L (%)	O_V (%)	O_C (%)
Co_3O_4 NCs	33	26.2	40.8
Co_3O_4 NSHDs	30.9	25.77	43.33
PdO-Co_3O_4 NSHDs	31	23.5	45.5

Figure 11 (a–c) XPS spectra of Co 2p in the Co_3O_4 NCs, Co_3O_4 NSHDs and PdO-Co_3O_4 NSHDs, respectively. (d) Fitting result of O 1s XPS spectra of above three samples.

high. Consequently, the selectivity of PdO-Co_3O_4 NSHDs is not very good and it can serve as a universal gas sensing material. The selectivity of PdO-Co_3O_4 NSHDs will be improved by doping or surface modification in the future.

Furthermore, the influence of relative humidity (RH) on the sensing performance was also investigated, as shown in Fig. S9. The RH has a little effect on the sensing performance of PdO-Co_3O_4 NSHDs. However, there is a trend that the sensing response decreases with the rise of RH, up to a minimum value, then increases with the rise of RH. This problem will be investigated in detail in the future.

The sensing characteristics of Co_3O_4, as a kind of p-type semiconductor, being same with n-type semiconductor, are affected by the surface reaction on the sensing layers (Fig. 10). However, the chemisorption of oxygen on Co_3O_4 creates the hole accumulation layer on the surface of Co_3O_4, different from that of n-type semiconductor [46–48], where the electron depletion layer is created at the grain boundaries. In general, the atmospheric oxygen is adsorbed in ionic forms at the surface as O_2^- (<100°C), O^- (100–300°C) and O^{2-} (>300°C) in the air [49]. Then, the TMA molecules as the reducing gas will interact with the chemisorbed oxygen (O^- and O_2^-) and donate free electrons to the sensing layers, which leads to the increase of resistance in the hole accumulation layer by the recombination of electrons and holes carriers. The possible reactions that take place on the surface of Co_3O_4 can be written as: $O_2(g) \rightarrow 2O^-_{(ads)} + 2h^+$ and $2N(CH_3)_{3(ads)} + 21O^-_{(ads)} \rightarrow N_2 + 9H_2O + 6CO_2 + 21e^-$.

First, the better TMA sensing performances of Co_3O_4 NSHDs compared to Co_3O_4 NCs can be attributed to the following reasons: (i) hollow structure, which enables gas molecules to diffuse both inside and outside of sensing layers; (ii) large surface areas and numerous mesopores, which can provide more active sites to improve the interaction of TMA molecules and Co_3O_4; (iii) ultrafine grains, which leads to a large variation of the hole accumulation layer resistance when Co_3O_4 reacts with the TMA molecules, resulting in a high gas sensing response. Second, the sensing performances of Co_3O_4 NSHDs are further improved by surface modification of the PdO NPs owing to the catalytic effect with PdO NPs that has been demonstrated in reported literature [40]. The PdO NPs can be partially reduced by TMA molecules because of the reduction of gases. Then, the reduction of PdO NPs can donate the free electrons to Co_3O_4 NSHDs, further decreasing the hole accumulation layers of Co_3O_4 NSHDs. These free electrons neutralized the holes in the Co_3O_4 NSHDs, leading to the increase of resistance in the PdO-Co_3O_4 NSHDs. Moreover, because the oxygen pressure in air can promise that PdO is the stable phase below 1,073 K, the reduced PdO NPs can be easily transferred to its oxidized state at 100°C, which ensures the reproducibility of the sensors.

In addition, Fig. 11a–c show the O 1s XPS spectra of Co_3O_4 NCs, Co_3O_4 NSHDs and PdO-Co_3O_4 NSHDs. Each asymmetric O 1s peak can be coherently fitted by three individual peaks. The O_L, O_V and O_C component of O 1s spectra is associated with the lattice oxygen, oxygen vacancies and chemisorbed oxygen species in the Co_3O_4 phase, respectively. Fig. 11d summarizes the relative percentage variation of each component on the surface of three samples. Noticeably, the PdO-Co_3O_4 NSHDs can adsorb more chemisorbed oxygen species than Co_3O_4

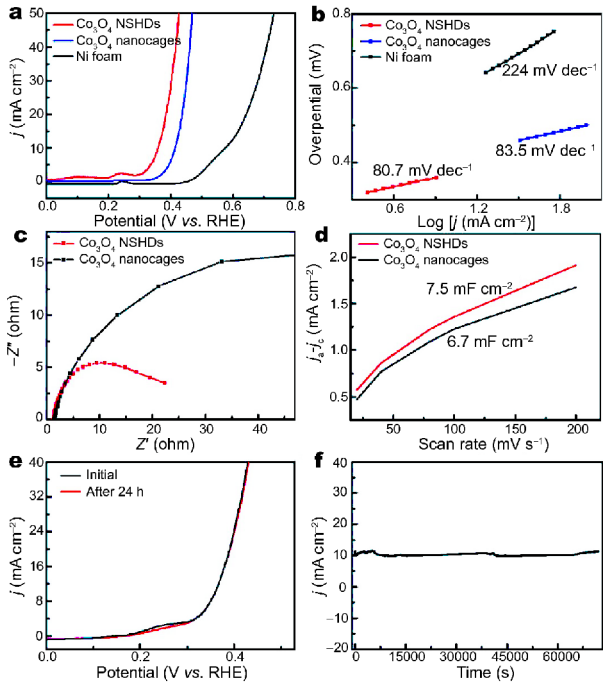

Figure 12 (a) LSV curves and (b) corresponding Tafel curves of Co_3O_4 NCs, Co_3O_4 NSHDs and Ni foam catalysts measured in 1.0 mol L^{-1} KOH. (c) EIS Nyquist plots. (d) Double-layer capacitance measurements. (e) LSV curves before and after 3,000 CV cycles. (f) Time-dependent current density curves for Co_3O_4 NSHDs in 1.0 mol L^{-1} KOH at constant potentials for 18 h.

NCs and Co_3O_4 NSHDs. Above results can explain why the sensing performances of PdO-Co_3O_4 NSHDs would be markedly enhanced.

The OER performances of the Co_3O_4 NSHDs were further tested in our case. Before conducting linear sweep voltammetry (LSV), the catalysts needed to be activated by cycling about 20 times of cyclic voltammetry (CV) until a stable CV curve [48]. From the LSV patterns (Fig. 12a), the Co_3O_4 NSHDs show an overpotential of 359 mV, which is 16 and 127 mV less than that of Co_3O_4 NCs and Ni foam, exhibiting the best OER catalytic performance among all the measurement samples. As shown in Fig. 12b, the Co_3O_4 NSHDs exhibit a small Tafel slope of 80.7 mV dec^{-1}, indicating its rapid OER reaction kinetics. Electrochemical impedance spectroscopy (EIS) was then performed to characterize the interface reactions and electrode kinetics. EIS of Co_3O_4 NCs and Co_3O_4 NSHDs were measured from 100 MHz to 0.01 Hz at an overpotential of 359 mV. From Fig. 12c, the Nyquist plots reveal that the semicircular diameter of Co_3O_4 NSHDs is obviously smaller than that of Co_3O_4 NCs, suggesting the lower charge transfer resistance and faster oxygen evolution rate.

In order to understand the apparent performance discrepancy about OER catalytic ability for the three catalysts, the electrochemical surface area (ECSA) was measured to evaluate the catalytic ability since a higher ECSA leads to more active sites (Fig. S10). Fig. 12d shows that the linear slope is 6.7 and 7.5 mF cm^{-2} for Co_3O_4 NCs and Co_3O_4 NSHDs, respectively. The Co_3O_4 NSHDs have a more electroactive surface, which corresponds to its enhanced reactivity. In addition to the high catalytic activity, the long-term stability of catalysts is also a key factor. As shown in Fig. 12e, no obvious reduction was found for the current density of the Co_3O_4 NSHDs catalyst after 3,000 CV cycling tests. In addition, the Co_3O_4 NSHDs have a static overpotential of 365 mV after continuous work for 10 h in 1.0 mol L^{-1} KOH at a steady current density of 10 mA cm^{-2} (Fig. 12f).

All of above results clearly demonstrate that the Co_3O_4 NSHDs can serve as a stable electrocatalyst and exhibit better catalytic performance than other samples. The enhanced OER activity of Co_3O_4 NSHDs may be attributed to the following reasons: (i) the large surface areas with numerous mesopores facilitate fast ions diffusion and high active loading [49–50,32]; (ii) the nanosheets with many ultrafine grains improve the transport/collection of charge carriers and thus the rapid charge transfer process [51]. We believe that the catalytic performances of the Co_3O_4 NSHDs could be further improved by surface modification or doping, which will be continued in the future.

CONCLUSION

In summary, the Co_3O_4 NSHDs were successfully synthesized by a two-step self-templated strategy. By this method, Co_3O_4 NSHDs with well-distributed PdO NPs were further obtained by the Pd modified Co-LDH HDs intermediate product based on controlled heating treatment. The prepared Co_3O_4 NSHDs have large surface areas, ultrathin nanosheets, ultrafine grains and numerous mesopores, which exhibit better sensing performance to TMA than Co_3O_4 NCs, and the PdO modified Co_3O_4 NSHDs further effectively enhanced the sensing performances for TMA, which have a low detection limit of 250 ppb and a short response time (4.5 s) and recovery time (12.5 s) at low operating temperature. More interestingly, the Co_3O_4 NSHDs exhibited excellent oxygen evolution reaction performances with a low overpotential of 359 mV, low Tafel slope of 80.7 mV dec^{-1} and low electrochemical impedance, which was superior to those from the Co_3O_4 NCs obtained by directly calcinating the ZIF-

67 templates, Ni foam and most common metal oxides catalysts. The Co_3O_4 NSHDs will be a good multi-functional material to achieve many applications. In addition, this material is also an ideal platform to realize enhancement of performances by further surface modification or doping.

Received 5 February 2018; accepted 19 March 2018; published online 16 April 2018

1 Zhang Y, Hsu BYW, Ren C, *et al.* Silica-based nanocapsules: synthesis, structure control and biomedical applications. Chem Soc Rev, 2015, 44: 315–335
2 Zhang G, Xu Y, Wang L, *et al.* Rational design of graphene oxide and its hollow CoO composite for superior oxygen reduction reaction. Sci China Mater, 2015, 58: 534–542
3 Yu Y, Zhang L, Wang J, *et al.* Preparation of hollow porous Cu_2O microspheres and photocatalytic activity under visible light irradiation. Nanoscale Res Lett, 2012, 7: 347
4 Yang H, Su Y, Ding L, *et al.* Rational synthesis of SnS_2@C hollow microspheres with superior stability for lithium-ion batteries. Sci China Mater, 2017, 60: 955–962
5 Song Y, Chen Y, Fu Y, *et al.* Hollow multicomponent zeolitic imidazolate frameworks-derived $3NiO{\cdot}2Ni_{3/2}Co_{1/2}ZnO_4$ for high rate lithium-ion batteries. J Alloys Compd, 2017, 703: 148–155
6 Tian K, Wang XX, Yu ZY, *et al.* Hierarchical and hollow Fe_2O_3 nanoboxes derived from metal–organic frameworks with excellent sensitivity to H_2S. ACS Appl Mater Interfaces, 2017, 9: 29669–29676
7 Jiang Y, Liu H, Tan X, *et al.* Monoclinic ZIF-8 nanosheet-derived 2D carbon nanosheets as sulfur immobilizer for high-performance lithium sulfur batteries. ACS Appl Mater Interfaces, 2017, 9: 25239–25249
8 Xing R, Zhou T, Zhou Y, *et al.* Creation of triple hierarchical micro-meso-macroporous n-doped carbon shells with hollow cores toward the electrocatalytic oxygen reduction reaction. Nano-Micro Lett, 2018, 10: 3
9 Yi JD, Shi PC, Liang J, *et al.* Porous hollow MoS_2 microspheres derived from core–shell sulfonated polystyrene microspheres@MoS_2 nanosheets for efficient electrocatalytic hydrogen evolution. Inorg Chem Front, 2017, 4: 741–747
10 Zhu Y, Kockrick E, Ikoma T, *et al.* An efficient route to rattle-type Fe_3O_4@SiO_2 hollow mesoporous spheres using colloidal carbon spheres templates. Chem Mater, 2009, 21: 2547–2553
11 Xu G, Otsubo K, Yamada T, *et al.* Superprotonic conductivity in a highly oriented crystalline metal–organic framework nanofilm. J Am Chem Soc, 2013, 135: 7438–7441
12 Zhao J, Quan X, Chen S, *et al.* Cobalt nanoparticles encapsulated in porous carbons derived from core–shell ZIF67@ZIF8 as efficient electrocatalysts for oxygen evolution reaction. ACS Appl Mater Interfaces, 2017, 9: 28685–28694
13 Xu G, Yamada T, Otsubo K, *et al.* Facile "modular assembly" for fast construction of a highly oriented crystalline MOF nanofilm. J Am Chem Soc, 2012, 134: 16524–16527
14 Yu Z, Bai Y, Liu Y, *et al.* Metal–organic-framework-derived yolk–shell-structured cobalt-based bimetallic oxide polyhedron with high activity for electrocatalytic oxygen evolution. ACS Appl Mater Interfaces, 2017, 9: 31777–31785
15 Jiang Z, Li Z, Qin Z, *et al.* LDH nanocages synthesized with MOF templates and their high performance as supercapacitors. Nanoscale, 2013, 5: 11770–11775
16 Jiang Z, Sun H, Qin Z, *et al.* Synthesis of novel ZnS nanocages utilizing ZIF-8 polyhedral template. Chem Commun, 2012, 48: 3620
17 Shao J, Wan Z, Liu H, *et al.* Metal organic frameworks-derived Co_3O_4 hollow dodecahedrons with controllable interiors as outstanding anodes for Li storage. J Mater Chem A, 2014, 2: 12194–12200
18 Wang Z, Jia W, Jiang M, *et al.* Microwave-assisted synthesis of layer-by-layer ultra-large and thin NiAl-LDH/RGO nanocomposites and their excellent performance as electrodes. Sci China Mater, 2015, 58: 944–952
19 Huang Y, Yu Y, Xin Y, *et al.* Promoting charge carrier utilization by integrating layered double hydroxide nanosheet arrays with porous $BiVO_4$ photoanode for efficient photoelectrochemical water splitting. Sci China Mater, 2017, 60: 193–207
20 Shao M, Ning F, Zhao J, *et al.* Preparation of Fe_3O_4@SiO_2@layered double hydroxide core–shell microspheres for magnetic separation of proteins. J Am Chem Soc, 2012, 134: 1071–1077
21 Li S, Cheng P, Luo J, *et al.* High-performance flexible asymmetric supercapacitor based on CoAl-LDH and rGO electrodes. Nano-Micro Lett, 2017, 9: 31
22 Dong C, Liu X, Wang X, *et al.* Hierarchical Ni/$NiTiO_3$ derived from NiTi LDHs: a bifunctional electrocatalyst for overall water splitting. J Mater Chem A, 2017, 5: 24767–24774
23 Zhang Y, Li C, Yu C, *et al.* Synthesis, characterization and activity evaluation of Cu-based catalysts derived from layered double hydroxides (LDHs) for DeNO_x reaction. Chem Eng J, 2017, 330: 1082–1090
24 Carrasco JA, Prima-Garcia H, Romero J, *et al.* CVD synthesis of carbon spheres using NiFe-LDHs as catalytic precursors: structural, electrochemical and magnetoresistive properties. J Mater Chem C, 2016, 4: 440–448
25 Gao Y, Zhang Z, Wu J, *et al.* Comprehensive investigation of CO_2 adsorption on Mg–Al–CO_3 LDH-derived mixed metal oxides. J Mater Chem A, 2013, 1: 12782–12790
26 Wen Z, Zhu L, Mei W, *et al.* Rhombus-shaped Co_3O_4 nanorod arrays for high-performance gas sensor. Sensor Actuat B-Chem, 2013, 186: 172–179
27 Wen Z, Zhu L, Li Y, *et al.* Mesoporous Co_3O_4 nanoneedle arrays for high-performance gas sensor. Sensor Actuat B-Chem, 2014, 203: 873–879
28 Wen Z, Zhu L, Mei W, *et al.* A facile fluorine-mediated hydrothermal route to controlled synthesis of rhombus-shaped Co_3O_4 nanorod arrays and their application in gas sensing. J Mater Chem A, 2013, 1: 7511–7518
29 Zhang Z, Zhu L, Wen Z, *et al.* Controllable synthesis of Co_3O_4 crossed nanosheet arrays toward an acetone gas sensor. Sensor Actuat B-Chem, 2017, 238: 1052–1059
30 Li Z, Lin Z, Wang N, *et al.* High precision NH_3 sensing using network nano-sheet Co_3O_4 arrays based sensor at room temperature. Sensor Actuat B-Chem, 2016, 235: 222–231
31 Song Z, Han X, Deng Y, *et al.* Clarifying the controversial catalytic performance of $Co(OH)_2$ and Co_3O_4 for oxygen reduction/evolution reactions toward efficient Zn–Air batteries. ACS Appl Mater Interfaces, 2017, 9: 22694–22703
32 Hang L, Sun Y, Men D, *et al.* Hierarchical micro/nanostructured C doped Co/Co_3O_4 hollow spheres derived from PS@$Co(OH)_2$ for the oxygen evolution reaction. J Mater Chem A, 2017, 5: 11163–11170

33 Yang X, Chen J, Chen Y, *et al.* Novel Co_3O_4 nanoparticles/nitrogen-doped carbon composites with extraordinary catalytic activity for oxygen evolution reaction (OER). Nano-Micro Lett, 2018, 10: 15

34 Qian J, Sun F, Qin L. Hydrothermal synthesis of zeolitic imidazolate framework-67 (ZIF-67) nanocrystals. Mater Lett, 2012, 82: 220–223

35 Xu C, Cao Y, Chen Y, *et al.* Fast synthesis of hierarchical $Co(OH)_2$ nanosheet hollow spheres with enhanced glucose sensing. Eur J Inorg Chem, 2016, 2016: 3163–3168

36 Lü Y, Zhan W, He Y, *et al.* MOF-templated synthesis of porous Co_3O_4 concave nanocubes with high specific surface area and their gas sensing properties. ACS Appl Mater Interfaces, 2014, 6: 4186–4195

37 Xiong S, Chen JS, Lou XW, *et al.* Mesoporous Co_3O_4 and CoO@C topotactically transformed from chrysanthemum-like $Co(CO_3)_{0.5}(OH)\cdot 0.11H_2O$ and their lithium-storage properties. Adv Funct Mater, 2012, 22: 861–871

38 Liu B, Zhang X, Shioyama H, *et al.* Converting cobalt oxide subunits in cobalt metal-organic framework into agglomerated Co_3O_4 nanoparticles as an electrode material for lithium ion battery. J Power Sources, 2010, 195: 857–861

39 Das R, Pachfule P, Banerjee R, *et al.* Metal and metal oxidenanoparticle synthesis from metal organic frameworks (MOFs): finding the border of metal and metal oxides. Nanoscale, 2012, 4: 591–599

40 Koo WT, Yu S, Choi SJ, *et al.* Nanoscale PdO catalyst functionalized Co_3O_4 hollow nanocages using MOF templates for selective detection of acetone molecules in exhaled breath. ACS Appl Mater Interfaces, 2017, 9: 8201–8210

41 Wang X, Ding B, Yu J, *et al.* Electro-netting: Fabrication of two-dimensional nano-nets for highly sensitive trimethylamine sensing. Nanoscale, 2011, 3: 911–915

42 Yang S, Liu Y, Chen W, *et al.* High sensitivity and good selectivity of ultralong MoO_3 nanobelts for trimethylamine gas. Sensor Actuat B-Chem, 2016, 226: 478–485

43 Park YH, Choi KJ, Bae JY, *et al.* Development of a detection sensor for mixed trimethylamine and ammonia gas. J Industrial Eng Chem, 2013, 19: 1703–1707

44 Park SH, Ryu JY, Choi HH, *et al.* Zinc oxide thin film doped with Al_2O_3, TiO_2 and V_2O_5 as sensitive sensor for trimethylamine gas. Sensor Actuat B-Chem, 1998, 46: 75–79

45 Zhang WH, Zhang WD. Fabrication of SnO_2–ZnO nanocomposite sensor for selective sensing of trimethylamine and the freshness of fishes. Sensor Actuat B-Chem, 2008, 134: 403–408

46 Song Z, Wei Z, Wang B, *et al.* Sensitive room-temperature H_2S gas sensors employing SnO_2 quantum wire/reduced graphene oxide nanocomposites. Chem Mater, 2016, 28: 1205–1212

47 Huang D, Yang Z, Li X, *et al.* Three-dimensional conductive networks based on stacked SiO_2@graphene frameworks for enhanced gas sensing. Nanoscale, 2017, 9: 109–118

48 Xu Z, Duan G, Kong M, *et al.* Fabrication of α-Fe_2O_3 porous array film and its crystallization effect on its H_2S sensing properties. ChemistrySelect, 2016, 1: 2377–2382

49 Jin H, Mao S, Zhan G, *et al.* Fe incorporated α-$Co(OH)_2$ nanosheets with remarkably improved activity towards the oxygen evolution reaction. J Mater Chem A, 2016, 5: 1078–1084

50 Chen Z, Zhao H, Zhang J, *et al.* IrNi nanoparticle-decorated flower-shaped $NiCo_2O_4$ nanostructures: controllable synthesis and enhanced electrochemical activity for oxygen evolution reaction. Sci China Mater, 2017, 60: 119–130

51 Wang X, Cao R, Zhang S, *et al.* Hierarchical flowerlike metal/metal oxide nanostructures derived from layered double hydroxides for catalysis and gas sensing. J Mater Chem A, 2017, 5: 23999–24010

Acknowledgements The authors acknowledge the financial support from the National Key R&D Program of China (2016YFC0201103), the Natural Science Foundation of China (51471161 and 11674320), and Youth Innovation Promotion Association CAS and Key Research Projects of the Frontier Science CAS (QYZDB-SSW-JSC017).

Author contributions All the authors make a general discussion.

Conflict of interest The authors declare no conflict of interest.

Supplementary information Supplementary information is available in the online version of the paper.

Yuanyuan Li received her BSc degree from Hefei University of Technology in 2015. She is currently pursing Master's degree in the University of Science and Technology of China. Her research is focused on the fabrication of nanomaterials and their gas sensing performances.

Guotao Duan received his BSc degree in Material Sciences from Heifei University of Technology in 2002. In 2007, he obtained a PhD in Materials Science from the Institute of Solid State Physics at the Chinese Academy of Sciences. He was a visiting scholar at the National Institute for Materials Science in Japan. Since 2007, he has been a professor at the Institute of Solid State Physics at the Chinese Academy of Sciences. His research interests include gas sensors based on the semiconductor micro/nanostructured array, detection devices, and the surface enhanced Raman spectrum of the noble metal micro/nanostructured array for environmental applications.

两步自模板法制备Co_3O_4纳米片基中空十二面体及其多功能应用

李圆圆[1,2], 刘波[1,2], 王弘[1,2], 苏星松[1,2], 高磊[1], 周飞[1], 段国韬[1*]

摘要 Co_3O_4纳米片基中空十二面体可以通过一种可控的自模板法制备而成. 首先利用ZIF-67为自模板合成Co-LDH中空十二面体, 然后将其作为自模板通过优化退火的方式制备Co_3O_4纳米片组成的中空十二面体(Co_3O_4 NSHDs). 利用该两步自模板法制得的Co_3O_4 NSHDs不仅具有中空结构、超薄的纳米片、超细的纳米颗粒, 还易实现表面的均匀修饰(如PdO的均匀修饰). 拥有上述特点的Co_3O_4 NSHDs可以实现多方面的应用, 例如气敏和催化. 实验结果表明Co_3O_4 NSHDs对三甲胺气体在低工作温度(100°C)下表现出很好的敏感特性. 在PdO表面修饰后, 对三甲胺的气敏性能进一步增强, 如更低的检测下限(250 ppb)和快速的气敏响应(4.5 s). 另外, 该材料也表现出优异的析氧反应活性. 和直接利用ZIF-67退火制得的Co_3O_4纳米笼、泡沫镍和大多数金属氧化物催化剂相比, 它具有较低的过电势(359 mV)、小的阻抗和小的塔菲尔斜率(80.7 mV dec^{-1}).

